IJMMM International Journal of Minerals, Metallurgy and Materials 矿物冶金与材料学报（英文版）

Microscopic damage evolution of anisotropic rocks under indirect tensile conditions: Insights from acoustic emission and digital image correlation techniques

Chaoqun Chu, Shunchuan Wu, Chaojun Zhang, and Yongle Zhang

Cite this article as:
Chaoqun Chu, Shunchuan Wu, Chaojun Zhang, and Yongle Zhang, Microscopic damage evolution of anisotropic rocks under indirect tensile conditions: Insights from acoustic emission and digital image correlation techniques, *Int. J. Miner. Metall. Mater.*, 30(2023), No. 9, pp. 1680-1691. https://doi.org/10.1007/s12613-023-2649-y

View the article online at SpringerLink or IJMMM Webpage.

International Journal of Minerals, Metallurgy and Materials
Volume 30, Number 9, September 2023, Page 1680
https://doi.org/10.1007/s12613-023-2649-y

Microscopic damage evolution of anisotropic rocks under indirect tensile conditions: Insights from acoustic emission and digital image correlation techniques

Chaoqun Chu[1,2], *Shunchuan Wu*[1,3)✉], *Chaojun Zhang*[1)], *and Yongle Zhang*[4)]

1) School of Civil and Resource Engineering, University of Science and Technology Beijing, Beijing 100083, China
2) Department of Civil & Mineral Engineering, University of Toronto, Toronto ON M5S 1A4, Canada
3) Faculty of Land Resources Engineering, Kunming University of Science and Technology, Kunmiing 650093, China
4) China Railway Sixth Group Limited Company, Beijing 100036, China
(Received: 4 August 2022; revised: 10 April 2023; accepted: 11 April 2023)

Abstract: The anisotropy induced by rock bedding structures is usually manifested in the mechanical behaviors and failure modes of rocks. Brazilian tests are conducted for seven groups of shale specimens featuring different bedding angles. Acoustic emission (AE) and digital image correlation (DIC) technologies are used to monitor the *in-situ* failure of the specimens. Furthermore, the crack morphology of damaged samples is observed through scanning electron microscopy (SEM). Results reveal the structural dependence on the tensile mechanical behavior of shales. The shale disk exhibits compression in the early stage of the experiment with varying locations and durations. The location of the compression area moves downward and gradually disappears when the bedding angle increases. The macroscopic failure is well characterized by AE event location results, and the dominant frequency distribution is related to the bedding angle. The *b*-value is found to be stress-dependent. The crack turning angle between layers and the number of cracks crossing the bedding both increase with the bedding angle, indicating competition between crack propagations. SEM results revealed that the failure modes of the samples can be classified into three types: tensile failure along beddings with shear failure of the matrix, ladder shear failure along beddings with tensile failure of the matrix, and shear failure along multiple beddings with tensile failure of the matrix.

Keywords: anisotropic rock; failure mechanism; acoustic emission; digital image correlation; Brazilian test

1. Introduction

With the change in world energy structure, increasing attention has been provided to the development and utilization of shale gas. Shale reservoirs typically demonstrate low porosity and permeability. The preferred orientation of minerals and the structural arrangement properties in the deposition process lead to their layered characteristics. The existence of bedding planes contributes to the remarkable variation of mechanical behavior, failure mode, and acoustic characteristics of shale along the bedding direction parallelly and perpendicularly [1–3]. Therefore, an accurate understanding of shale's mechanical behavior, crack evolution characteristics, and final failure mode is of considerable importance and can provide theoretical support for shale gas exploitation and the construction of anisotropic rock projects.

Most experimental results of anisotropic rock show that the uniaxial compressive strength (UCS) [4–5], Brazilian tensile strength (BTS) [6–7], and triaxial compressive strength (TCS) [7–8] are dependent on the variation of anisotropic characteristics. Hoek [9] reported the tensile strength parallel to the bedding plane was substantially larger than that perpendicular to the bedding plane. Niandou *et al*. [10] discussed the variation in elastic parameters, plastic deformation, and failure mode of shale under different confining pressures. Liu *et al*. [11] found that the tensile strength, elastic modulus, and wave velocity of shale decreased with the increase in bedding angle; moreover, the compressive strength and Poisson ratio demonstrated the law of U-type change. Simpson *et al*. [12] studied the effect of Mancos shale bedding on crack initiation and propagation. Jin *et al*. [13] conducted uniaxial compression, direct tensile, and Brazilian tests on Marcellus shale and found that the change in bedding angle induced an anisotropy effect on static mechanical behavior. Gao *et al*. [14] performed a series of Brazilian splitting tests on printed gypsum-based similar rocks using 3D printing technology to study the effect of printing orientation on their tensile properties.

The study of mechanical behavior alone is insufficient to understand the failure of anisotropic rock, which must be further explored in failure characteristics and failure mode.

Investigations on the crack evolution characteristics of an-

✉ Corresponding author: Shunchuan Wu Email: wushunchuan@ustb.edu.cn

isotropic rock continuously expand with the update in experimental technology and equipment. Many studies have analyzed the influence of anisotropic characteristics from crack initiation [15–18], micro-crack evolution [19–21], crack type [22–25], and crack turning mechanism [26]. The increase in bedding angle usually has a considerable impact on the crack type and propagation mode. The development mechanism of cracks and the internal crack relationship needs further study. Vervoot *et al*. [27] analyzed the effect of bedding angle on tensile strength and the type of failure mode through Brazilian splitting tests on anisotropic rocks. Li *et al*. [28] conducted a direct tensile test of shale and found a layered effect of failure mode; however, rather than pure tensile fracture, four different failure modes were observed. Feng *et al*. [29] studied the Brazilian splitting test of shale under different loading rates. The influence of shale anisotropy on the failure of the sample gradually decreased with the increase in the loading rate. In the study of the dynamic behavior of the Brazilian disk sample, Wu *et al*. [30] investigated the tensile properties of Brazilian disk rock materials in combination with dynamic splitting tests. The Young's modulus of the three stages of the sample under the dynamic load condition is obtained, and the failure mechanism of the Brazilian disk is analyzed during the three stages. Han *et al*. [31] used dynamic impact tests to ascertain the dynamic behavior of sandstone disks with coplanar elliptical flaws and combined digital image correlation (DIC) and scanning electron microscopy (SEM) to demonstrate the relationship between dynamic mechanical parameters and fracture behavior. Wu *et al*. [32] studied the dynamic tensile failure of rocks under static pre-tension and found that the tensile strength significantly increased with the loading rate but was insensitive to pre-tension. Huang *et al*. [33] used a new integrated real-time loading–observation–acquisition system to observe the meso-failure process of continental shale in the Ordos Basin, China. The internal mechanism is revealed from the above research to a certain extent, but the exploration of the failure mode in the classification of macroscopic failure, crack evolution, and competition mechanism remains unclear.

Acoustic emission (AE) monitoring and DIC technology are also used to monitor and characterize the failure characteristics of anisotropic rocks. The variation in AE characteristic parameters and temporal and spatial evolutions of AE events are often used to analyze the failure evolution characteristics of anisotropic rocks [34–36]. DIC, which has a simple and efficient setting, is typically used to record the failure mode [37] and strain evolution [38–39] of anisotropic samples and monitor the crack evolution process during the test [40]. Li *et al*. [41] and Wu *et al*. [42] used AE monitoring and DIC technology with a split Hopkinson pressure bar system to study the influence of anisotropic characteristics on crack propagation evolution quantitatively. Li *et al*. [43–44] investigated the size effect of anisotropic rocks and found that the sample size, loading–stripping angle, and loading configuration jointly controlled the failure mechanism of transversely isotropic rock. Dan *et al*. [45] analyzed the stress distribution and failure mode of transversely isotropic samples under Brazilian test conditions through numerical simulation and analytical solution, concluding that anisotropic characteristics and loading direction both strongly affected the failure mode of samples.

The research on anisotropic rocks focused on the influence of anisotropic characteristics on tensile strength [46–48] in the early period. Thus, the study of crack propagation of anisotropic rocks and the classification of failure modes gradually attracted the attention of researchers. The influence of anisotropic characteristics on failure was comprehensively understood using AE and DIC technology, but the crack propagation and failure modes of anisotropic rocks remained unclear, with considerable space for further exploration. Therefore, the Longmaxi shale from southern Sichuan Province of China was tested in this study under the Brazilian test conditions. Based on the combination of whole-process AE and DIC monitoring and SEM technology, the strain field, dominant frequency, AE event location, AE magnitude, and SEM image were collected together to analyze the mechanical behavior of shale, crack evolution characteristics, and final failure mode and reveal the relationship between the bedding plane and the matrix in the failure process.

2. Experimental

2.1. Preparation of sample

The shale samples are characterized by their black appearance and bedding structure. The average density of the sample was 2.55 g·cm^{-3}, and the porosity was 3.41%. SEM images (Fig. 1(a) and (b)) and X-ray diffraction (XRD) pattern (Fig. 1(c)) show that the samples mainly mineral comprise 51.18wt% quartz, 28.51wt% clay minerals (kaolinite and illite), 11.08wt% feldspar, 4.41wt% carbonate minerals

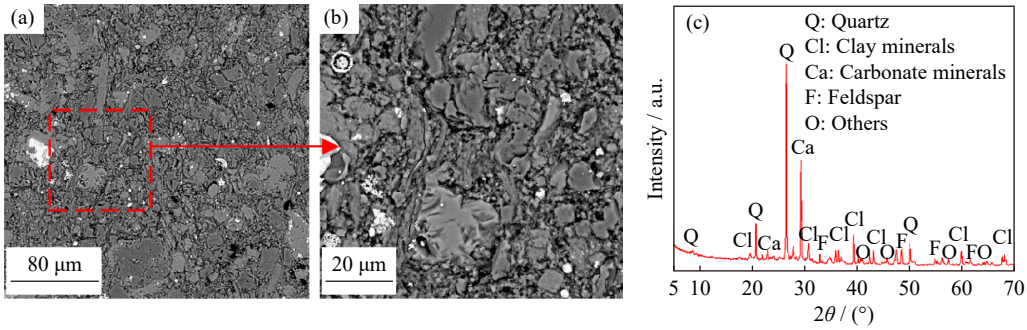

Fig. 1. (a, b) SEM images and (c) XRD pattern of the shale.

(calcite, dolomite), and other minerals. The overall heterogeneity of the mineral arrangement was strong. Through ultrasonic velocity measurements from different sample directions, the wave velocity perpendicular and parallel to the bedding plane was 3696 and 3182 $m \cdot s^{-1}$, respectively. Longmaxi shale can be regarded as a transversely isotropic material.

The shale samples were processed into the standard disk samples recommended by the International Society for Rock Mechanics and Rock Engineering (ISRM), which has a size of 50 mm in diameter and 25 mm in height, ensuring that the parallelism of the upper and lower end faces was controlled within ±0.02 mm. The end face was perpendicular to the axis of the sample, and the deviation was not more than 0.25°. The angle between the loading direction and the plane where the bedding plane located is defined as the bedding angle (α), as shown in Fig. 2(a). Fig. 2(b) is the speckle processed sample. The sample is taken from the same rock block and then processed, as shown in Fig. 2(c), because the test is passive acoustic emission monitoring of shale with bedding, named as BP-0, BP-15, BP-30, BP-45, BP-60, BP-75, and BP-90. Two sets of experiments were set up, two samples were conducted at each angle, and one set of samples was arranged for AE and DIC monitoring.

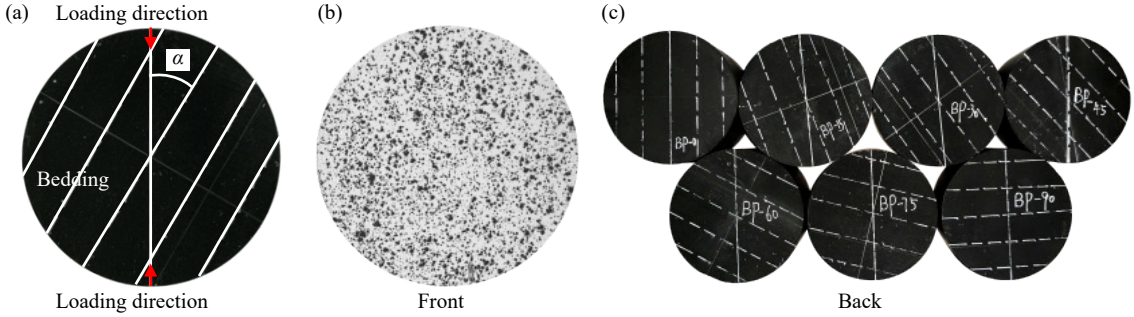

Fig. 2. Typical specimen photos: (a) schematic of the Brazil test on shale disk; (b) speckle finished; (c) set of samples.

2.2. Mechanical testing and AE and 3D–DIC system

This test adopts the indirect measurement method of rock tensile strength recommended by the ISRM, and the equipment is a YAW-600 electrohydraulic servo testing machine. The minimum resolution of the testing machine was 3 N. A simplified ISRM-recommended method was used for the Brazilian splitting test under a linear load condition. Additionally, a device that closely approximates linear load conditions was designed. The effectiveness of this self-designed equipment for Brazilian test results was verified on the basis of previous research [49–50]. Compared to uniformly distributed, sinusoidal, parabolic loads, and linear load can produce a similar stress field in most of the disk specimen areas. A self-designed loading device was used to arrange eight AE sensors and monitor DIC synchronously during the experiment, as shown in Fig. 3(a).

DIC is an optical testing method based on experiments that can obtain surface displacement information by tracking and calculating the spatial positions of surface particles with characteristic gray gradient information during the loading period. Before loading, $f(x)$ is taken as the reference system, and a point (x_0, y_0) is selected as the center of a region of interest. A certain searching method is then used to perform a correlation operation in the deformed image $g(x', y')$ according to a predetermined correlation function. Captured images were processed by VIC-3D software [31]. The DIC full-field strain measurement requires spraying speckles on the circular surface of the disk sample; therefore, a thin and uniform white primer is sprayed on the surface of the sample. The speckle is characterized by uniform and randomly distributed irregular dots, as shown in Fig. 2(b).

Mechanical disturbances at the sample surface, which are caused by the synthetic sources or the microcracks, can be detected during the test procedure and outputted as a voltage by the high frequency piezoelectric sensors. As the electrical signal traveled to the analog-to-digital acquisition card, amplifier units with built-in bandpass filters were used as preamplifiers to amplify raw AE signals. The amplified analog signals were then continuously digitized and recorded by the continuous acquisition system. The AE signal acquisition system, a 12-channel continuous acquisition system, can synchronously acquire the active and passive waveform signals during the experiment (Fig. 3(b)). Each Richter[16] unit can sample four channels synchronously at a sampling frequency of 10 MHz and digitize the waveforms at a 12-bit resolution. The AE sensor is a PICO sensor from the American Physical Acoustics Corporation, with a center frequency of 550 kHz and a frequency range of 200–750 kHz. Pulser amplifier desktop units with 0.1 Hz–1 MHz bandpass filters are used, and the gain range is 30–70 dB.

The layout of the eight sensors is shown in Fig. 3(c), where in the front and rear surfaces of the disk sample are 8 mm, and the sensors are evenly distributed on the cylindrical surface at 45°. The sensors are fixed in advance on the sample using a self-designed fluorine rubber tube base to reduce the attenuation and dissipation of AE signals between the sensor and the sample contact surface, and silicone grease was evenly applied between the sensor and the sample contact surface as a coupling agent, improving the quality of signal acquisition. The odd- and even-numbered gain values are set to 30 and 50 dB [50], respectively (High gain values can effectively collect micro-fracture information and help study crack nucleation, penetration, and quasistatic propagation

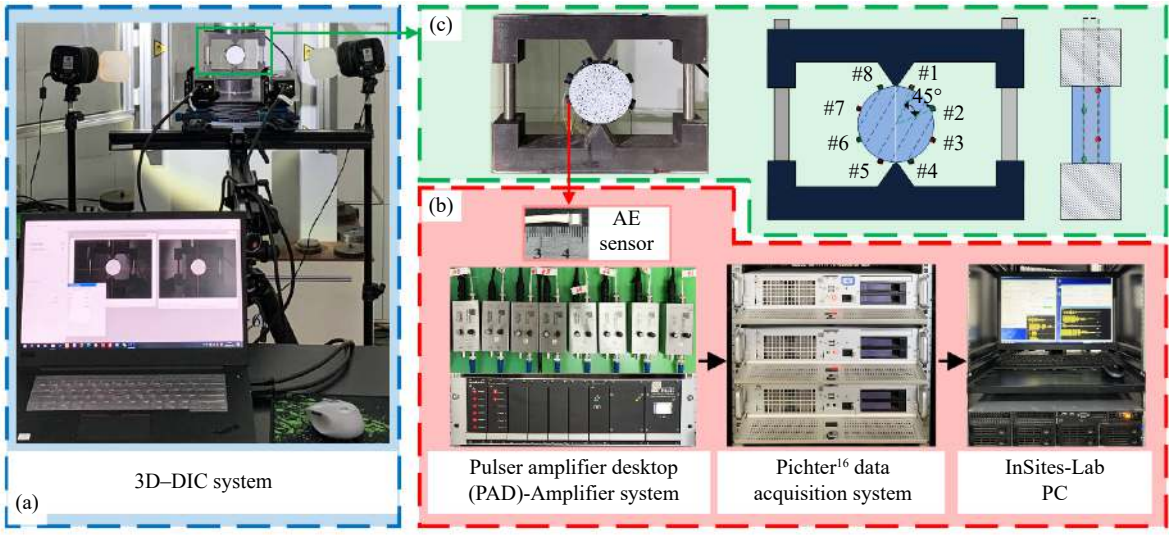

Fig. 3. Experiment equipment and process diagram: (a) 3D–DIC system; (b) photograph of the AE monitoring system (Pulser Interface Unit, Triple 4-channel Richter[16] continuous acquisition system, Processing PC); (c) schematic of the AE sensor layout, wherein eight PICO sensors (Nos. 1–8) were placed on the disk circumference.

processes. Low-gain values reduce peak clipping and effectively obtain important information on the final crack propagation stage).

The loading system, the DIC monitoring, and the AE acquisition system were simultaneously turned on during the experiment, and the force on the sample was loaded at a rate of 30 $N \cdot s^{-1}$ under the linear quasistatic loading condition to the failure of the sample.

3. Results

3.1. Mechanical characteristic

The Brazilian test is widely used in tensile strength experiments due to the convenience of sample preparation and test process. The tensile stress is generated in the center of the disk through the diameter compression of the rock disk. The disk splits when the tensile stress reaches the tensile strength of the material. Theoretically, the tensile strength (σ_t) can be expressed as [51]:

$$\sigma_t = \frac{P}{\pi R t}$$

where P is the load at both ends of the disk sample diameter, R is the disk radius, and t is the disk thickness. The assumption of a two-dimensional plane must be satisfied using the preceding formula, and the disk is considered to be uniform and isotropic elastic material that satisfies the center crack initiation condition. However, the samples in this experimental do not have isotropic properties; therefore, this calculated value cannot represent the true tensile strength.

The loading force–time curve is drawn in accordance with a set arranged with AE and DIC monitoring, as shown in Fig. 4. The curve fluctuation of BP-90 is caused by the special failure mode of the sample, and the statistical experiment parameters of all samples are listed in Table 1. Fig. 5 shows the maximum loading force and the curve fits well through the quadratic polynomial. The failure of shale

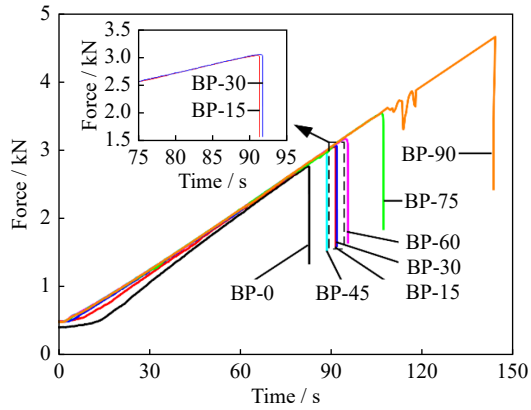

Fig. 4. Force–time curves of shale disk under Brazilian test.

Table 1. Data of Brazilian test on shales

No.	t / mm	D / mm	P_{max} / kN	σ_t / MPa
BP0-1	25.07	50.08	2.78	1.41
BP0-2	25.05	50.04	2.64	1.33
BP15-1	25.16	50.09	3.06	1.55
BP15-2	25.10	50.07	3.01	1.56
BP30-1	25.12	50.08	3.08	1.56
BP30-2	25.11	48.99	3.05	1.58
BP45-1	25.09	48.97	2.98	1.52
BP45-2	25.03	50.07	3.18	1.61
BP60-1	25.13	50.08	3.18	1.61
BP60-2	25.03	50.02	3.28	1.66
BP75-1	25.03	49.01	3.55	1.84
BP75-2	25.05	50.04	3.65	1.85
BP90-1	24.95	50.05	4.17	2.12
BP90-2	25.05	50.07	4.07	2.07

Notes: D represents diameter; P_{max} represents the maximum force.

samples under Brazilian conditions is significantly affected by the bedding dip angle. During the change in the bedding

angle from 0° to 90°, the nominal σ_t showed a positive correlation and rising trend, and the average σ_t increased from 1.37 to 2.10 MPa, demonstrating an increase of 52.54%, which is different from the failure characteristics of layered rock under uniaxial compression [4].

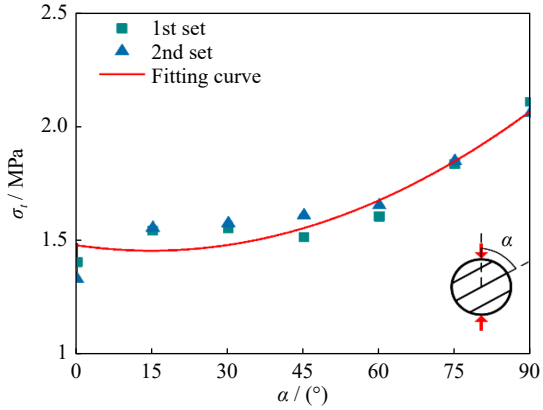

Fig. 5. Variation of σ_t orientation of the bedding angle.

The σ_t of two sets of samples is drawn in Fig. 5. σ_t and the growth rate continued to rise with the increase in the bedding angle. The σ_t difference slightly changes when α = 30° and 45°, and the overall trend demonstrated a pronounced structure-dependent anisotropy and is associated with failure modes in different bedding angles.

3.2. Principal strain field evolution

DIC technology uses the image before deformation as a reference, meshes the research area, regards each sub-area as a rigid motion, and calculates the correlation between strain and displacement of the sub-area according to a predefined correlation function through the certain search algorithm. The collected results of this study were imported into the VIC-3D software for analysis. Based on the DIC technology, the software can process data with a minimum resolution of 5×10^{-6}, and the strain measurement range is 0.005%–2000%. The major parameters of the DIC include subset size (29 pixel × 29 pixel), step size (6 pixel × 6 pixel), and strain window size (8 pixel × 8 pixel).

A screenshot of the x–y plane showing the e_1-Lagrange strain was exported, and results of four different stages ($0.5\sigma_t$, $0.9\sigma_t$, $0.95\sigma_t$, and σ_t) were taken (Fig. 6). The blue dotted line on the sample failure photo is the indicator line parallel to the bedding, while the red dotted line is the sketch line of the failure surface. The areas that demonstrate a large value of the maximum principal strain are known as the large maximum principal strain (LMPS) regions, which can be used as important evidence to predict the surface failures of rocks [52].

The evolution region of LMPS shows that the main strain evolution region distribution on the 0° sample is relatively uniform in the entire sample except near the loading contact region when the loading force is $0.5\sigma_t$. Coalescence appeared along the loading direction under a loading force of $0.95\sigma_t$. The LMPS region further expanded when the loading force was $0.95\sigma_t$. The predicted sample will be destroyed along the loading direction when σ_t is reached. For the samples with α = 15°–75°, when the loading force reaches $0.5\sigma_t$, $0.9\sigma_t$, and $0.95\sigma_t$, the evolution region of LMPS regions is highly similar to that of the 0° sample. The obviously similar performance was particularly observed on the 30°, 60°, and 75° specimens, simultaneously producing microcracks in the interior. However, the final failure surface trace indicates that the sample does not fail along the loading direction, which is successfully verified in the discussion of the SEM results. For the sample with a 90° bedding angle, the behavior of $0.5\sigma_t$ and $0.9\sigma_t$ is consistent with the above findings. Meanwhile, the final failure mode at $0.95\sigma_t$ and σ_t cannot be predicted by DIC monitoring, and the final failure photos of the sample are consistent with this finding. The evolution of the LMPS region demonstrates anisotropic characteristics. All the obtained results and analysis of Brazilian tests through DIC technology reveal that the LMPS region is in the center of the sample in the early stage of the test and passes through the loading direction. With the increase in the loading force, the correlation between the evolution of the LMPS region and the bedding angle becomes prominent and no longer exists along the loading direction.

3.3. AE localization

The maximum amplitude of background noise was not more than 5 mV during the experiment. Therefore, the channel with a gain of 30 dB uses 5 mV as the threshold, while that with a gain of 50 dB uses 10 mV as the threshold to trigger the continuous AE signal. In the trigger process, if the waveform amplitude from no less than four channels exceeds the threshold, then the waveform data of 204.8 ms are recorded and stored. This phenomenon is identified as an AE event. The arrival time of the P-wave is obtained by root mean square (RMS) auto-picking algorithm methods, and the collapsing grid search algorithm is used for source localization analysis. The event location patterns of the samples with bedding angles of 15°–75° are similar; thus, samples with α = 0°, 45°, and 90° are taken to draw the projection of the location results in three directions (Fig. 7). The color and size of the event display are drawn in accordance with the location magnitude and the signal-to-noise ratio of the signal, respectively.

From the typical AE localization results, in the failure of the 0° sample, the large AE events are distributed at the loading area without large main nucleation aggregation areas. This distribution is due to the failure occurrence parallel to the bedding in the sample under a low-level stress state and the presence of some tiny cracks inside the sample during the loading process. Location results of the 45° sample also show that the different bedding angles lead to different failures under the Brazilian test. However, the location results of the 90° sample are mainly concentrated in two regions. The line connecting the two nucleation regions is in the diameter direction of the sample and parallel to the bedding plane. This phenomenon is attributed to the formation of the macroscop-

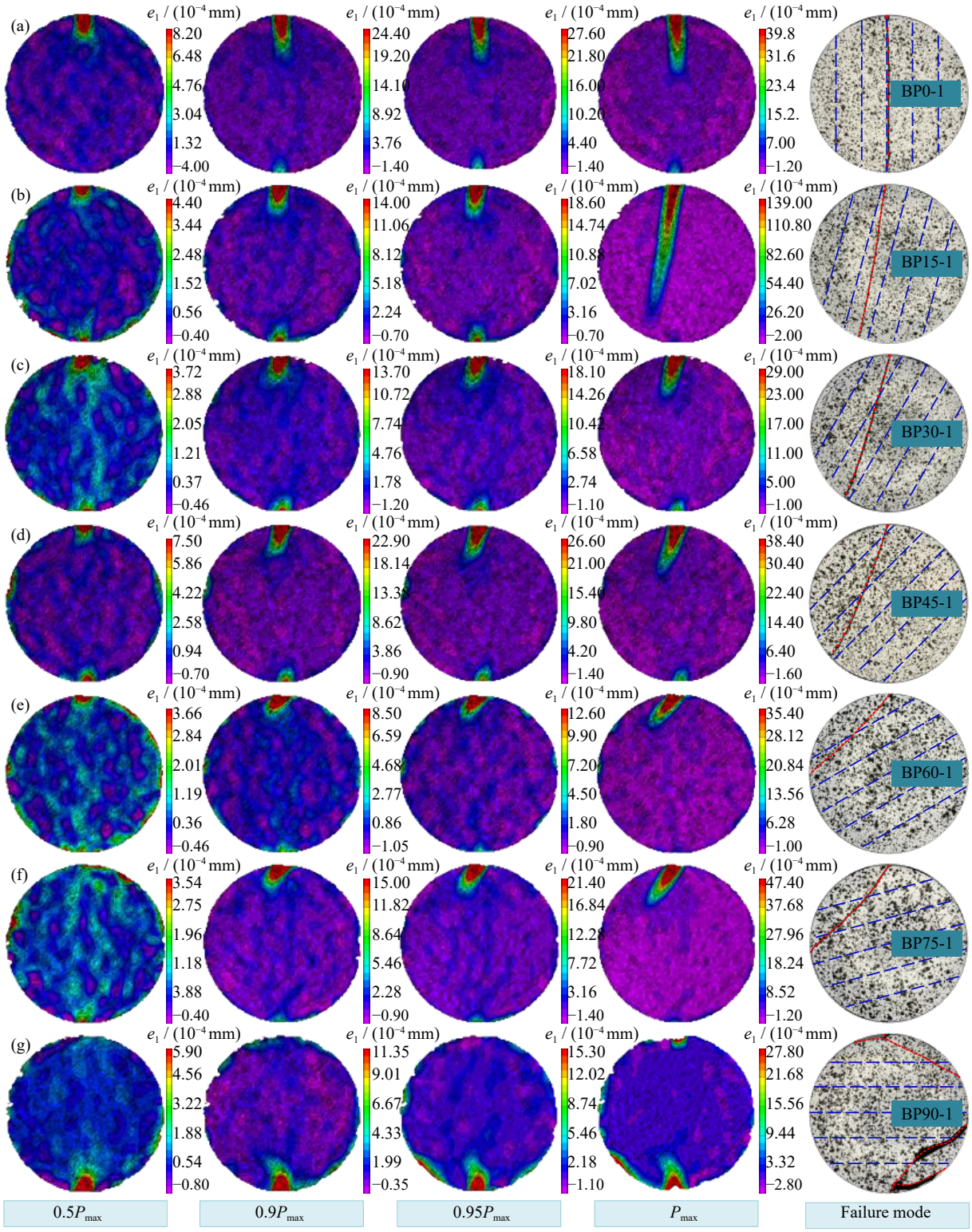

Fig. 6. Strain (e_1-Lagrange) evolution and failure mode of shale disk under Brazilian test.

ic surface in the interior before the final failure during the loading process of the 90° sample due to the loading direction perpendicular to the inner layer. Meanwhile, the sensor dropped due to the area caused by the failure, and the final instantaneous AE event is not monitored to locate the nucleation stage. The analysis of the AE location magnitude revealed that the 90° sample is larger than the two other samples, which is consistent with the final failure strength and severity of the sample.

4. Discussion

4.1. AE frequency characteristics

The AE waveform is converted by fast Fourier transform calculation after denoising, obtaining a two-dimensional spectrum of the extracted waveform. The frequency corresponding to the maximum amplitude point in the two-dimensional spectrum is determined as the dominant frequency of the event waveform. According to the frequency response

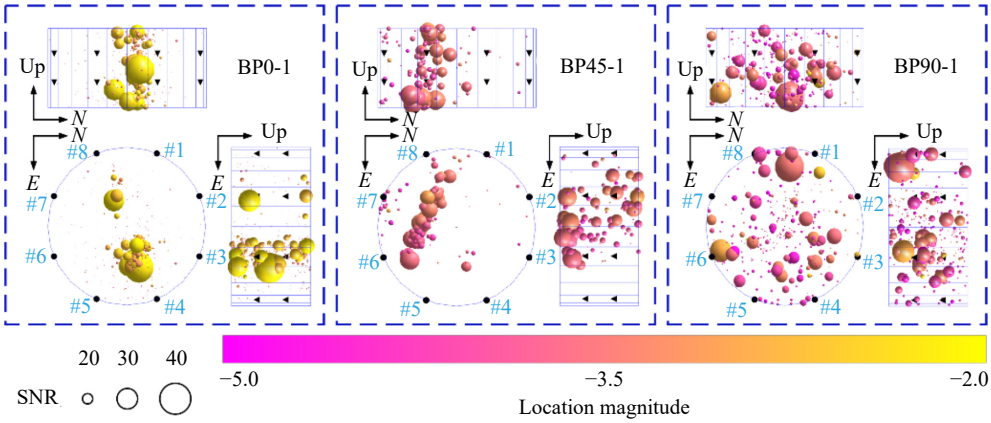

Notes: SNR represents the signal of noise ratio; *N* represents North; *E* represents East.

Fig. 7. AE localization results of the typical samples.

characteristics of the PICO sensor used in this study, the frequency range of the sensor is mainly divided into three frequency bands [53]: low-frequency signal (less than 200 kHz), intermediate frequency signal (200–500 kHz), and high-frequency signal (more than 500 kHz). Fig. 8(a)–(g) shows the distribution of dominant frequencies in the entire failure process of the sample, while Fig. 8(h) shows the proportion of the dominant frequency signals of each sample based on the statistical results. Almost no high frequency signal is observed when α = 30°, 45°, and 60°, and the dominant frequency distribution is concentrated. The high frequency signal gradually increased under 15°, 75°, and 90°, and the overall distribution shows the U type with the increase of α. The proportion of intermediate frequency signals is the highest at 0°, 30°, and 60°. Simultaneously, an increasing trend of low frequency signals is revealed in Fig. 8(h).

4.2. Magnitude distribution of AE signals (*b*-value)

The *b*-value is calculated on the basis of the power law distribution of AE events [54]. The magnitude of the AE event ranges from −5 to −1.5, and the distribution interval is 0.1 with increasing α from 0° to 90°. The *b*-value is calculated as 0.9639, 1.4662, 1.2995, 1.4276, 0.9460, 0.8042, and 0.8107. Fig. 9 shows the relationship between the σ_t and *b*-value. The *b*-value decreases with the increase in σ_t, indicating a negative correlation and a certain stress dependence relationship between σ_t and *b*-value. The dependence of the *b*-value on the variation in the anisotropic structure is also proven.

4.3. Strain feature analysis

Three virtual extensometers are centrally arranged along the loading direction on the surface of the sample according to the DIC monitoring results to further explore the stress change and distribution of the sample during the failure process (three identical red fine rectangles marked in Fig. 10). The No. 1 extensometer (E1) is $\frac{1}{6}D$ away from the upper edge, the No. 2 extensometer (E2) is in the center of the sample, and the No. 3 extensometer (E3) is $\frac{1}{6}D$ from the bottom (D represents the diameter of the sample). The schematic of the extensometer arrangement is shown in Fig. 10.

The data of the three extensometers for each sample are drawn in an image, filling the area between the data line and the coordinate axis, as shown in Fig. 11(a)–(g). The 0°–45° samples have a compression process in the early stage of the experiment. E1 compression plays a dominant role in the early compression process of 0° and 15° samples, that is, the upper part of the sample. The compression of the 30° sample appeared in E2, which is close to the position of the sample center. At a 45° bedding angle, the compression is mainly produced at the E3 position and lasts for a long period. However, the compression phenomenon rarely emerged in the 60° and 75° samples. Compression behavior is only observed in the early stage of the experiment of the 90° sample. With the increase in α, the compression area shifts downward, and the compression phenomenon disappears. The strain results monitored by the three extensometers during sample failure are plotted in Fig. 11(h). The result of the E1 extensometer demonstrates the most fluctuation, whose value is largest when α = 0° and 45°. The value of E1 is also the largest in 0° and 45° samples. The E2 and E3 extensometers decrease first and then increase, while E1 changes greatly in the 45° and 75° samples, and the overall trend is the fluctuation decreases.

4.4. Failure mode and crack propagation characteristics

The damaged samples were made into SEM probe slides, which were observed through a Phenom XL SEM. The pictures were spliced in accordance with the moving order to obtain the clearest crack pictures with a wide field of view, as shown in Fig. 12. The white virtual line refers to the direction of the bed plane.

The above careful analysis of the cracks showed that the changes in the loading force and failure time are consistent with that of the angle and continue to increase. The roughness of the failure surface of the sample also has the same regulation. For the 0° sample, the crack types are divided into tensile failure between layers and shear fracture and tensile failure between layers. A ladder failure mode mixed with the shear slip failure between layers and the tensile fracture of the bedding itself mainly occurs in the 15° sample. The 30°, 45°,

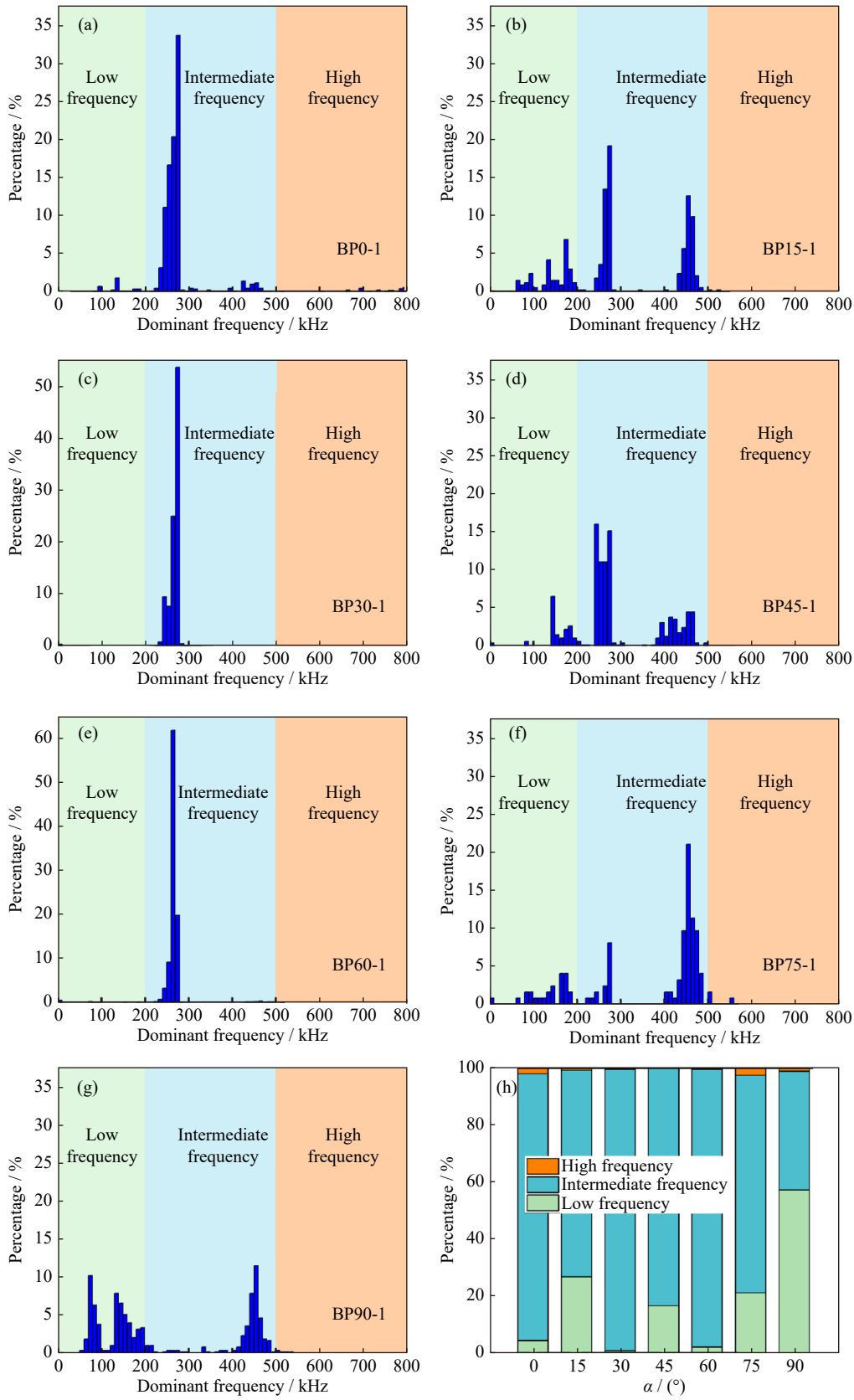

Fig. 8. Frequency distribution characteristics: (a–g) dominant frequency of AE signals at different bedding angles; (h) proportion of three frequency components.

60°, and 75° samples not only induced ladder-like failure mode (same as 15 samples) but also contributed to cracks (preferentially developed but not penetrated along the bedding), which are crossed with the final failure surface, particularly on the 45° sample. The tensile fracture angle of the layer itself expands with the increase in the bedding angle; that is, the crack turning angle (CTA) between the layer and the interlayer and the number of cracks crossing bedding

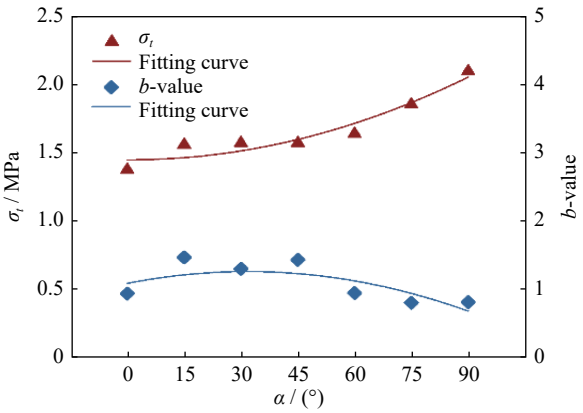

Fig. 9. Relationship between b-values and the σ_t of the sample.

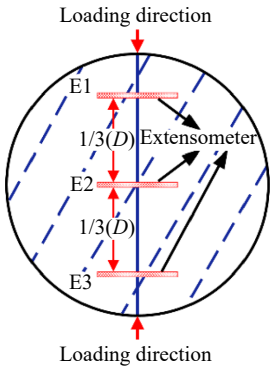

Fig. 10. DIC virtual extensometer layout.

(NCCB) both increase. The failure modes of samples can be classified into three types: tensile failure along beddings with shear failure of the matrix (0° and 90°), ladder shear failure along beddings with tensile failure of the matrix (mainly shear failure, 15°, 30°, 45°, 60°, and 75°), and shear failure and shear multiple beddings with tensile failure of the matrix (30°, 45°, 60°, and 75°).

According to the crack evolution results of DIC, combined with the SEM image, the cracks of the sample start with small ones (affected by the bedding, such as the 45° sample) rather than proceeding along the initially monitored crack mode. As the loading force increases, the competition mechanism of cracks emerges while the development along the bedding plane decreases. The tiny cracks originally developed along the bedding plane cannot completely form large cracks (i.e., the macrocracks). Macrocracks are formed by the crack with a tensile shear effect. This phenomenon is consistent with the analysis result, which shows that the ladder crack tends to gain considerable complexity, and the NCCB tends to rise.

As a special type of rock, shale has a clear layered structure based on the SEM analysis of the specimens in the experimental preparation section (Section 2.1). Therefore, the anisotropic behavior of shale fractures was observed in the Brazilian splitting test. This finding is attributed to the matrix and weak planes of the shale, which comprise different mineral particles and pores, and the different distribution directions and shapes of these particles and pores in various directions. Different mineral particles and pores in various directions in the rock sample will exhibit different stress responses when the load is applied due to the change in the laminated angle α. In the Brazilian splitting test, the stress field is the largest in the load direction along the specimen diameter, which leads to the initiation and propagation of cracks. Simultaneously, the stress is minimum in the vertical direction of the specimen, which limits the crack propagation rate. These factors generally contribute to the anisotropic behavior of shale in the Brazilian splitting test. Shale is known to exhibit significant anisotropic behavior; that is, its properties can vary depending on its testing direction. This condition can have important implications for the results of tensile tests using the Brazilian disk method because the loading direction can impact the observed failure behavior.

4.5. Relationship between the macroscopic fracture surface and bedding direction

The angle between the failure surface and the loading direction is defined as β, while that between the failure surface and the bedding direction is defined as θ. The detailed results

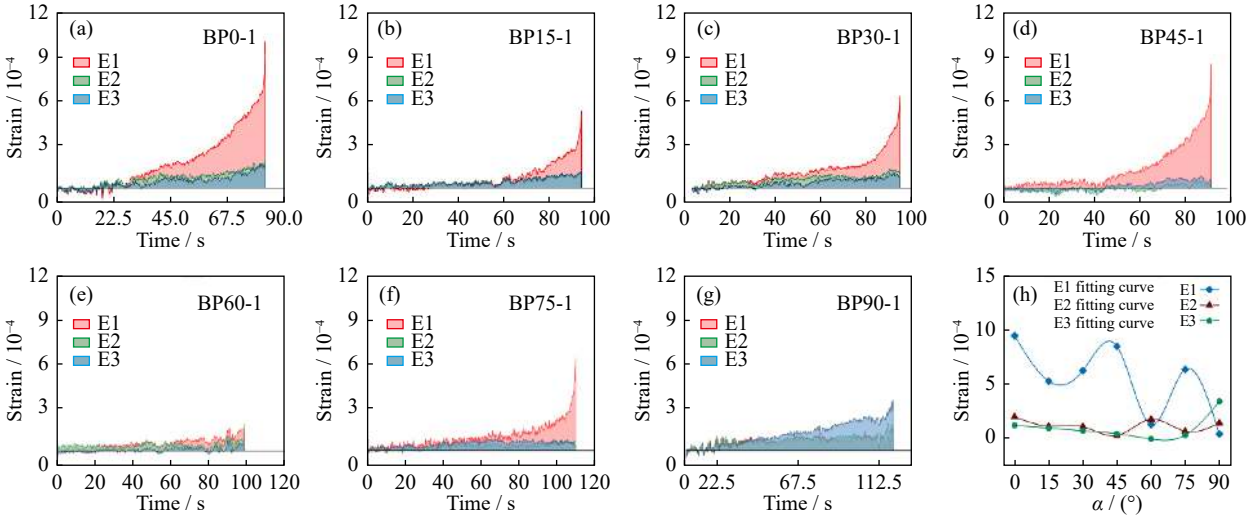

Fig. 11. DIC virtual extensometer showing strain results: (a–g) the strain change of each sample in the whole process; (h) the strain value at the time of failure.

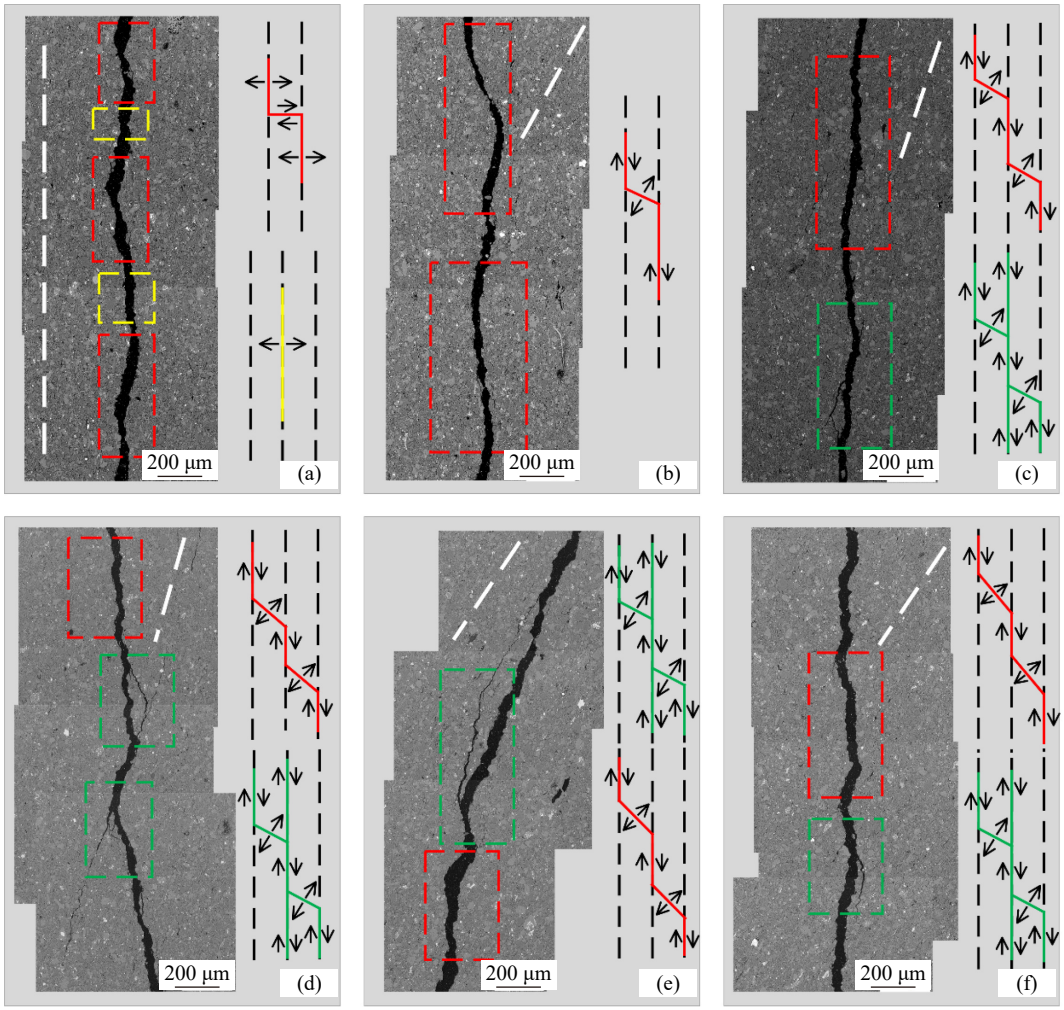

Fig. 12. SEM images of shale disks with different bedding angles and schematic of crack classification: (a) BP0-1; (b) BP15-1; (c) BP30-1; (d) BP45-1; (e) BP60-1; (f) BP75-1 (The white dotted line is the direction parallel to the bedding plane, and the yellow, red, and green dotted line frames correspond to the same color crack type diagram shown on the right side).

are shown in Table 2.

When $\alpha = 90°$, the value of β and θ are the average of the three failure surfaces. With the increase in the bedding angle, β gradually rises, and the anisotropic characteristics of the shale demonstrate a significant impact on the failure procedure. The results verified that the combination of the above different failure modes leads to a significant positive correlation between the formation of the macroscopic failure surface and the anisotropy of shale, which has layered structure dependence from the aforementioned phenomenon, as shown in Fig. 13.

Table 2. Macroscopic fracture surface data statistics

α / (°)	β / (°)	θ / (°)
0	0	0
15	10.1	4.9
30	17.7	13.4
45	23.8	21.2
60	45.0	15.0
75	42.1	32.9
90	66.2	35.8

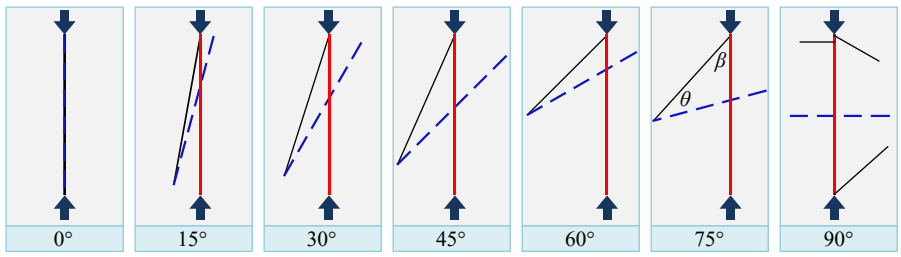

Fig. 13. Schematic of macroscopic fracture, loading direction, and bedding angle of the shale sample (The arrow and red solid lines refer to the loading direction, the blue dotted line and black solid line refer to the bedding plane direction and failure surface, respectively).

5. Conclusions

The Brazilian test of shale was conducted in this study, and AE and DIC were used to monitor the entire process. The layered structure characteristics of shale lead to anisotropic characteristics of mechanical behavior, AE characteristics, and failure mode in the failure process. The microscopic mechanism of shale failure is analyzed by SEM images, the relationship between the bedding plane and matrix in the failure process was revealed, and the competition mechanism and variation law of cracks were discovered, which can provide some valuable insights into understanding the tensile failure of anisotropic rocks effectively. The conclusions were presented as follows.

(1) As α increases, σ_t exhibits a parabolic growth trend and is notably dependent on the layered structure. The DIC monitoring results indicate that the evolution of the LMPS region displays apparent anisotropic characteristics. As the loading force increases, the relationship between the evolution of the LMPS region and α becomes increasingly apparent, which is no longer consistent with the loading direction.

(2) The results of AE localization are consistent with the final failure mode of the sample. The *b*-value decreases with the increase in the σ_t, showing a negative correlation. A certain stress dependence is observed, which also proves the dependence of the *b*-value on the anisotropic structure.

(3) The shale disk has a compression stage at the beginning of the experiment, and the compression area and duration are different. The location of the compression area shifts downward with the increase in α, and the compression phenomenon disappears.

(4) With the increase in bedding angle, the tensile crack angle of the layer expands; that is, the CTA between the layer and the interlayer increases, and so does the NCCB. With the increase in the loading force, the competition mechanism of cracks emerges while the crack development along the bedding plane decreases. The macrocracks are formed by cracks with a tensile shear effect.

Acknowledgements

Thanks for the help from Dr. Yusong Zhao. This work is financially supported by the National Natural Science Foundation of China (No. 51934003) and the Major Science and Technology Special Project of Yunnan Province, China (Nos. 202102AF080001 and 202102AG050024).

Conflict of Interest

Shunchuan Wu is the editorial board member for this journal and was not involved in the editorial review or the decision to publish this article. The authors declare that they have no known competing financial interests or personal relationships that could have appeared to influence the work reported in this paper.

References

[1] C.D. Martin, S. Giger, and G.W. Lanyon, Behaviour of weak shales in underground environments, *Rock Mech. Rock Eng.*, 49(2016), No. 2, p. 673.

[2] C.M. Sayers, The effect of anisotropy on the Young's moduli and Poisson's ratios of shales, *Geophys. Prospect.*, 61(2013), No. 2, p. 416.

[3] G. Khanlari, B. Rafiei, and Y. Abdilor, An experimental investigation of the Brazilian tensile strength and failure patterns of laminated sandstones, *Rock Mech. Rock Eng.*, 48(2015), No. 2, p. 843.

[4] C.Q. Chu, S.C. Wu, S.H. Zhang, P. Guo, and Z. Min, Mechanical behavior anisotropy and fracture characteristics ofbedded sandstone, *J. Cent. South Univ.*, 51(2020), No. 8, p. 2232.

[5] T.Z. Zhang, H.G. Ji, X.B. Su, *et al*., Evaluation and classification of rock heterogeneity based on acoustic emission detection, *Int. J. Miner. Metall. Mater.*, 29(2022), No. 12, p. 2117.

[6] J.W. Cho, H. Kim, S. Jeon, and K.B. Min, Deformation and strength anisotropy of Asan gneiss, Boryeong shale, and Yeoncheon schist, *Int. J. Rock Mech. Min. Sci.*, 50(2012), p. 158.

[7] S.Q. Yang, P.F. Yin, B. Li, and D.S. Yang, Behavior of transversely isotropic shale observed in triaxial tests and Brazilian disc tests, *Int. J. Rock Mech. Min. Sci.*, 133(2020), art. No. 104435.

[8] S. Lozovyi and A. Bauer, From static to dynamic stiffness of shales: Frequency and stress dependence, *Rock Mech. Rock Eng.*, 52(2019), No. 12, p. 5085.

[9] E. Hoek, Fracture of anisotropic rock, *J. S. Afr. Inst. Min. Metall.*, 64(1964), No. 10, p. 510.

[10] H. Niandou, J.F. Shao, J.P. Henry, and D. Fourmaintraux, Laboratory investigation of the mechanical behaviour of Tournemire shale, *Int. J. Rock Mech. Min. Sci.*, 34(1997), No. 1, p. 3.

[11] Q. Liu, B. Liang, W.J. Sun, and H. Zhao, Experimental study on the difference of shale mechanical properties, *Adv. Civ. Eng.*, 2021(2021), p. 1.

[12] N.D.J. Simpson, A. Stroisz, A. Bauer, A. Vervoort, and R.M. Holt, Failure mechanics of anisotropic shale during Brazilian tests, [in] *Proceedings of the 48th US Rock Mechanics/Geomechanics Symposium*, Minneapolis, 2014.

[13] Z.F. Jin, W.X. Li, C.R. Jin, J. Hambleton, and G. Cusatis, Anisotropic elastic, strength, and fracture properties of Marcellus shale, *Int. J. Rock Mech. Min. Sci.*, 109(2018), p. 124.

[14] Y.T. Gao, T.H. Wu, and Y. Zhou, Application and prospective of 3D printing in rock mechanics: A review, *Int. J. Miner. Metall. Mater.*, 28(2021), No. 1, p. 1.

[15] G.W. Xu, C. He, Z.Q. Chen, and A. Su, Transverse isotropy of phyllite under Brazilian tests: Laboratory testing and numerical simulations, *Rock Mech. Rock Eng.*, 51(2018), No. 4, p. 1111.

[16] Z. Aliabadian, G. Zhao, and A. Russell, Failure, crack initiation and the tensile strength of transversely isotropic rock using the Brazilian test, *Int. J. Rock Mech. Min. Sci.*, 122(2019), art. No. 104073.

[17] X.M. Yin, X. Zhang, Y.J. Lei, and L.N. Wang, Effect of loading direction on the critical characteristic strength and energy evolution of quartz mica schist and microscale mechanisms, *Bull. Eng. Geol. Environ.*, 80(2021), No. 11, p. 8693.

[18] P. Li, M.F. Cai, P.T. Wang, Q.F. Guo, S.J. Miao, and F.H. Ren, Mechanical properties and energy evolution of jointed rock specimens containing an opening under uniaxial loading, *Int. J. Miner. Metall. Mater.*, 28(2021), No. 12, p. 1875.

[19] M. Sakha, M. Nejati, A. Aminzadeh, S. Ghouli, M.O. Saar, and T. Driesner, On reliable prediction of fracture path in anisotropic rocks, *Procedia Struct. Integr.*, 39(2022), p. 792.

[20] L. Yang, M. Sharafisafa, and L.M. Shen, On the fracture mechanism of rock-like materials with interbedded hard-soft layers under Brazilian tests, *Theor. Appl. Fract. Mech.*, 116(2021), art. No. 103102.
[21] P. Xu, R.S. Yang, J.J. Zuo, *et al*., Research progress of the fundamental theory and technology of rock blasting, *Int. J. Miner. Metall. Mater.*, 29(2022), No. 4, p. 705.
[22] Y.Y. Meng, H.W. Jing, X.W. Liu, Q. Yin, L. Zhang, and H.X. Liu, Experimental and numerical investigation on the effect of bedding plane properties on fracture behaviour of sandy mudstone, *Theor. Appl. Fract. Mech.*, 114(2021), art. No. 102989.
[23] C.D. Ding, Y. Zhang, D.W. Hu, H. Zhou, and J.F. Shao, Foliation effects on mechanical and failure characteristics of slate in 3D space under Brazilian test conditions, *Rock Mech. Rock Eng.*, 53(2020), No. 9, p. 3919.
[24] S. Na, W. Sun, M.D. Ingraham, and H. Yoon, Effects of spatial heterogeneity and material anisotropy on the fracture pattern and macroscopic effective toughness of Mancos Shale in Brazilian tests, *J. Geophys. Res.*, 122(2017), No. 8, p. 6202.
[25] H. Wang, Y. Li, S.G. Cao, *et al*., Fracture toughness analysis of HCCD specimens of Longmaxi shale subjected to mixed mode I-II loading, *Eng. Fract. Mech.*, 239(2020), art. No. 107299.
[26] X.W. Yang, X.P. Zhang, Q. Zhang, C.D. Li, and D.J. Wang, Study on the mechanisms of crack turning in bedded rock, *Eng. Fract. Mech.*, 247(2021), art. No. 107630.
[27] A. Vervoort, K.B. Min, H. Konietzky, *et al*., Failure of transversely isotropic rock under Brazilian test conditions, *Int. J. Rock Mech. Min. Sci.*, 70(2014), p. 343.
[28] C.B. Li, B.B. Zou, H.W. Zhou, and J. Wang, Experimental investigation on failure behaviors and mechanism of an anisotropic shale in direct tension, *Geomech. Geophys. Geo-Energy Geo-Resour.*, 7(2021), No. 4, art. No. 98.
[29] G. Feng, Y. Kang, X.C. Wang, Y.Q. Hu, and X.H. Li, Investigation on the failure characteristics and fracture classification of shale under Brazilian test conditions, *Rock Mech. Rock Eng.*, 53(2020), No. 7, p. 3325.
[30] N. Wu, J.Y. Fu, Z.D. Zhu, and B. Sun, Experimental study on the dynamic behavior of the Brazilian disc sample of rock material, *Int. J. Rock Mech. Min. Sci.*, 130(2020), art. No. 104326.
[31] Z.Y. Han, D.Y. Li, and X.B. Li, Experimental study on the dynamic behavior of sandstone with coplanar elliptical flaws from macro, meso, and micro viewpoints, *Theor. Appl. Fract. Mech.*, 120(2022), art. No. 103400.
[32] R. Chen and K.W. Xia, Dynamic tensile failure of rocks under static pre-tension, *Int. J. Rock Mech. Min. Sci.*, 80(2015), p. 12.
[33] B.X. Huang, L.H. Li, Y.F. Tan, R.L. Hu, and X. Li, Investigating the meso-mechanical anisotropy and fracture surface roughness of continental shale, *J. Geophys. Res.*, 125(2020), No. 8, art. No. e2019JB017828.
[34] B. Debecker and A. Vervoort, Experimental observation of fracture patterns in layered slate, *Int. J. Fract.*, 159(2009), No. 1, p. 51.
[35] J. Wang, L.Z. Xie, H.P. Xie, *et al*., Effect of layer orientation on acoustic emission characteristics of anisotropic shale in Brazilian tests, *J. Nat. Gas Sci. Eng.*, 36(2016), p. 1120.
[36] Y. Li, L. Xue, and X.W. Wu, Study on acoustic emission and X-ray computed-tomography characteristics of shale samples under uniaxial compression tests, *Environ. Earth Sci.*, 78(2019), No. 5, p. 1.
[37] P.F. Yin and S.Q. Yang, Experimental investigation of the strength and failure behavior of layered sandstone under uniaxial compression and Brazilian testing, *Acta Geophys.*, 66(2018), No. 4, p. 585.
[38] V. Kramarov, P.N. Parrikar, and M. Mokhtari, Evaluation of fracture toughness of sandstone and shale using digital image correlation, *Rock Mech. Rock Eng.*, 53(2020), No. 9, p. 4231.
[39] M. Sharafisafa and L.M. Shen, Experimental investigation of dynamic fracture patterns of 3D printed rock-like material under impact with digital image correlation, *Rock Mech. Rock Eng.*, 53(2020), No. 8, p. 3589.
[40] S.Q. Yang, P.F. Yin, and Y.H. Huang, Experiment and discrete element modelling on strength, deformation and failure behaviour of shale under Brazilian compression, *Rock Mech. Rock Eng.*, 52(2019), No. 11, p. 4339.
[41] J. Li, J. Zhao, H.C. Wang, K. Liu, and Q.B. Zhang, Fracturing behaviours and AE signatures of anisotropic coal in dynamic Brazilian tests, *Eng. Fract. Mech.*, 252(2021), art. No. 107817.
[42] R.J. Wu, H.B. Li, and D.P. Wang, Full-field deformation measurements from Brazilian disc tests on anisotropic phyllite under impact loads, *Int. J. Impact Eng.*, 149(2021), art. No. 103790.
[43] K.H. Li, Z.Y. Yin, D.Y. Han, X. Fan, R.H. Cao, and H. Lin, Size effect and anisotropy in a transversely isotropic rock under compressive conditions, *Rock Mech. Rock Eng.*, 54(2021), No. 9, p. 4639.
[44] K.H. Li, Y. Cheng, Z.Y. Yin, D.Y. Han, and J.J. Meng, Size effects in a transversely isotropic rock under Brazilian tests: Laboratory testing, *Rock Mech. Rock Eng.*, 53(2020), No. 6, p. 2623.
[45] D.Q. Dan and H. Konietzky, Numerical simulations and interpretations of Brazilian tensile tests on transversely isotropic rocks, *Int. J. Rock Mech. Min. Sci.*, 71(2014), p. 53.
[46] D.W. Hobbs, The tensile strength of rocks, *Int. J. Rock Mech. Min. Sci. Geomech. Abstr.*, 1(1964), No. 3, p. 385.
[47] K. Barron, Brittle fracture initiation in and ultimate failure of rocks, *Int. J. Rock Mech. Min. Sci. Geomech. Abstr.*, 8(1971), No. 6, p. 565.
[48] G. Barla and N. Innaurato, Indirect tensile testing of anisotropic rocks, *Rock Mech.*, 5(1973), No. 4, p. 215.
[49] D.Y. Li and L.N.Y. Wong, The Brazilian disc test for rock mechanics applications: Review and new insights, *Rock Mech. Rock Eng.*, 46(2013), No. 2, p. 269.
[50] S.H. Zhang, S.C. Wu, G. Zhang, P. Guo, and C.Q. Chu, Three-dimensional evolution of damage in sandstone Brazilian discs by the concurrent use of active and passive ultrasonic techniques, *Acta Geotech.*, 15(2020), No. 2, p. 393.
[51] Z.T. Bieniawski and I. Hawkes, Suggested methods for determining tensile strength of rock materials, *Int. J. Rock Mech. Min. Sci. Geomech. Abstr.*, 15(1978), No. 3, p. 99.
[52] Y.S. Zhao, C.C. Chen, S.C. Wu, P. Guo, and B.L. Li, Effects of 2D&3D nonparallel flaws on failure characteristics of brittle rock-like samples under uniaxial compression: Insights from acoustic emission and DIC monitoring, *Theor. Appl. Fract. Mech.*, 120(2022), art. No. 103391.
[53] P. Guo, S.C. Wu, G. Zhang, and C.Q. Chu, Effects of thermally-induced cracks on acoustic emission characteristics of granite under tensile conditions, *Int. J. Rock Mech. Min. Sci.*, 144(2021), art. No. 104820.
[54] B. Gutenberg and C.F. Richter, Frequency of earthquakes in California, *Bull. Seismol. Soc. Am.*, 34(1944), No. 4, p. 185.